International Journal of Design & Nature and Ecodynamics
Vol. 21, No. 4, April, 2026, pp. 915-927
Journal homepage: http://iieta.org/journals/ijdne

# Effect of Pyrolysis Temperature on the Properties of *Gnetum gnemon* Shell biochar and Its Methylene Blue Adsorption Performance

Hidayat Hidayat[1], Fera Arum[1*], Santi Ari Respati[1], Wiwiek Dwi Susanti[1], Faidliyah Nilna Minah[2], Dwi Ana Anggorowati[2], Ali Rahmat[1]

[1] National Research and Innovation Agency, Jakarta 10340, Indonesia
[2] Department of Chemical Engineering, Institut Teknologi Nasional Malang, Malang 65143, Indonesia

Corresponding Author Email: fera001@brin.go.id



https://doi.org/10.18280/ijdne.210402

**Received:** 12 January 2026
**Revised:** 16 April 2026
**Accepted:** 26 April 2026
**Available online:** 30 April 2026

***Keywords:***
*adsorption, biochar, gnemon shell biomass, methylene blue, pyrolysis, wastewater treatment, waste valorization*

**ABSTRACT**

Biochar derived from *Gnetum gnemon* shell was systematically investigated to elucidate the effect of pyrolysis temperature on its physicochemical evolution and adsorption performance toward methylene blue (MB). Pyrolysis was conducted at 350, 450, 550, and 650 °C for 4 h, followed by comprehensive characterization (proximate analysis, Scanning Electron Microscopy (SEM), Brunauer-Emmett-Teller (BET) surface area, Fourier transform infrared (FTIR), X-ray diffraction (XRD), and Thermogravimetric Analysis (TGA)) and batch adsorption (variation of MB concentration). Yield declined sharply with temperature (48.47% at 350 °C to 35.15% at 650 °C), concomitant with decreases in volatile matter (34.65% to 7.62%), hydrogen (3.8% to 1.41%), oxygen (14.03% to 5.93%), and O/C ratio (0.206-0.080), while fixed carbon increased 1.46-fold from 47.66 to 69.86%, elemental C increased from 67.84 to 74.36, and aromaticity increased. SEM revealed a morphological transformation from compact to highly porous matrices; the BET surface area increased 74.9-fold from 1.84 to 137.98 $m^2/g$, and the pore volume increased 3.7-fold from 0.032 to 0.1197 $cm^3/g$. FTIR indicated progressive loss of hydroxyl and carbonyl groups, while XRD confirmed enhanced graphitic ordering with distinct peaks at $2\theta = 22°$ and 43°. TGA demonstrated higher residual mass (33.7% at 650 °C) and improved thermal stability. The higher the removal capacity, the higher GSB-650 is at each initial MB concentration, while GSB-350 is the lowest. The removal capacity of GSB-650 is 1.2-2.4 times greater than that of GSB-350. The adsorption capacity increases with the increasing pyrolysis temperature. GSB-650 biochar has the highest adsorption capability across all concentrations, while GSB-350 has the lowest. The Maximum adsorption capacity was found at GSB-650 with a value of 9.28 mg/g. Isothermal matching with Langmuir-type monolayer chemisorption with $R^2 > 0.9$ for GSB-350 and GSB-650. Gnemon shell biochar is a promising low-cost adsorbent for dye removal. Due to its low efficiency, activation or functionalization is required to improve performance and expand its applications in environmental remediation.

## 1. INTRODUCTION

The increasing demand for essential products has driven industrial expansion across sectors such as chemicals, pharmaceuticals, agriculture, and textiles. While this diversification supports economic growth [1], it also poses environmental challenges that affect soil and water quality [2]. Notably, the textile industry significantly contributes to water contamination through dyeing processes that utilize toxic chemicals [3]. The textile industry accounts for approximately 17-20% of industrial water pollution, largely from dyeing processes that release harmful chemicals such as ammonia, sulfides, and lead [4]. Effluents from dyeing contain high levels of total dissolved solids (TDS), chemical oxygen demand (COD), and biochemical oxygen demand (BOD), which are detrimental to aquatic ecosystems [5].

Synthetic dyes like methylene blue (MB) are prevalent for their vibrant colors but are difficult to degrade, leading to severe ecological consequences [6]. Even at low concentrations, they reduce water transparency, disrupt photosynthesis, deplete oxygen, and harm aquatic life [7]. Dye contamination is also linked to health issues such as skin irritation and neurological disorders [8]. To address dye contamination, various remediation methods have been explored, including adsorption, photocatalytic degradation, ionic flocculation, coagulation, and oxidation [9, 10]. Among these, adsorption is recognized as an effective, cost-efficient, and environmentally friendly approach for dye removal [11]. In contrast, other methods, such as photocatalytic degradation and oxidation, often require complex operational conditions, high energy inputs, or generate potentially harmful by-products, limiting their practical application in large-scale wastewater treatment. Given these limitations, adsorption has gained increasing attention due to its operational simplicity,

reusability of materials, and minimal secondary pollution. Among various adsorbents studied, carbon-based materials such as biochar have emerged as particularly promising. Biochar, a carbon-rich material produced via pyrolysis, offers a combination of high surface area, porous structure, and abundant functional groups, making it an excellent adsorbent for water contaminants [12]. Numerous studies have shown that biochar effectively removes phenolic compounds, dyes, and heavy metals [13, 14].

*Gnetum gnemon* L. (*melinjo*), an indigenous Indonesian plant, generates significant shell waste during processing that remains largely underutilized [15]. The structural composition of gnemon shells, rich in cellulose, hemicellulose, and lignin, makes them promising raw materials for activated carbon production [16]. These properties suggest that gnemon shells are well-suited for biochar production, offering a sustainable method to valorize waste materials.

The adsorption capacity of biochar is influenced by several key factors, including pore size, surface area, and the presence of functional groups. Other contributing parameters, such as pyrolysis temperature, surface chemistry, and pH conditions, are also widely recognized for their significant roles in enhancing adsorption performance [17, 18]. Higher pyrolysis temperatures typically increase biochar's aromaticity, surface area, and adsorption capacity for contaminants like simazine [19]. Thus, optimizing pyrolysis conditions is essential to producing biochar with tailored characteristics for enhanced adsorption efficiency.

This study investigated (i) how pyrolysis temperature affects the physicochemical properties (yield, Brunauer-Emmett-Teller (BET) surface area, pore volume, pore size, functional groups, carbon content) of biochar derived from gnemon shells and (ii) determined the optimal pyrolysis temperature that produces biochar with the best adsorption performance. This aims to develop effective adsorbents for water remediation while promoting sustainable waste utilization.

## 2. METHODS

### 2.1 Preparation of biochars

The dried *Gnetum gnemon* shell was chopped into small and uniform sizes (around 10 mesh), then dried in an oven at 105 ℃ for 24 h to remove moisture, and then cooled to room temperature. Furthermore, the sample was put into a porcelain cup with a lid until full, then weighed to obtain the initial weight (raw weight). The cup containing the gnemon shell was then wrapped in aluminum foil to limit the presence of oxygen during the pyrolysis process. The pyrolysis process was carried out by inserting the cup into the furnace and heating it for 4 hours at temperature variations of 350, 450, 550, and 650 ℃. After the pyrolysis process was complete, the biochar was cooled naturally in the furnace to room temperature. The biochar from pyrolysis at each of these temperatures was coded GSB-350, GSB-450, GSB-550, and GSB-650. The cooled sample was then crushed and sieved using a 60-mesh sieve. The fraction that passed the sieve was used for the analysis of characteristics and the adsorption process.

### 2.2 Characterization of biochars

The parameters observed in this study include: (1) percentage of biochar yield, calculated based on the ratio of biochar mass to the mass of the initial raw material; (2) biochar surface morphology analyzed using Scanning Electron Microscopy (SEM), Thermo Scientific Quattro S FESEM NETZSCH STA 449F3 Simultaneous, the analysis was performed at an accelerating voltage of 3 kV. Images were obtained at a magnification of 2,000×., with Scale bar 50 μm; (3) identification of functional groups using Fourier transform infrared (FTIR) spectra were recorded between 4000 and 400 $cm^{-1}$ in an optical cuvette with a resolution of 4 $cm^{-1}$ and taking 16 scans at 25 ℃; background correction was performed before each measurement using PerkinElmer Spectrum; (4) crystal structure characterization carried out using X-ray diffraction (XRD) 7000 Shimadzu American Standard Testing Method; XRD analysis was performed using Cu Kα radiation (λ = 1.5406 Å) operated at 40 kV and 30 mA. The diffraction data were collected in the 2θ range of 10–80° using a continuous scan mode at a scanning rate of 2°/min with a step size of 0.0189°. and (5) Thermal Analyzer, analysis of biochar thermal stability using Thermogravimetric Analysis (TGA), TGA was performed under a nitrogen ($N_2$) atmosphere with a gas flow rate of 20 mL/min. The samples were heated from 25 ℃ to 1000 ℃ at a heating rate of 10 ℃/min. Measure BET surface using a Quantachrome Nova 4200e analyzer, where samples were degassed at 250 ℃ for 3 hours before analysis. Adsorbent: Nitrogen gas ($N_2$) at 77 K, then calculated the BET surface area between a relative pressure ($P/P_0$) of 0.05–0.30 BJH method was used to obtain the pore size distribution.

In addition, proximate analysis was also carried out, which included water, ash, and volatile matter content based on the American Standard for Testing and Materials (ASTM) D3173 (moisture), D3174 (ash), and D3175 (volatile matter) methods. Meanwhile, ultimate analysis to determine the content of elements such as carbon, hydrogen, nitrogen, and sulfur was carried out by referring to the ASTM D3573 or D5373 (carbon, hydrogen, and nitrogen) and D4239 (sulfur) standards.

### 2.3 Batch adsorption experiment

Batch adsorption experiments were carried out by adding 0.15 g of each of the four types of biochar into a 50 mL conical flask with different concentrations (20, 40, 60, 80 mg/L) of MB. Furthermore, 50 mL of MB solution was added to each flask. The mixture was then shaken using a tube roller at a speed of 80 rpm for 4 hours. After the adsorption process was complete, the solution was filtered using a syringe filter with a pore size of 0.45 microns to separate the biochar particles. The filtrate obtained was then analyzed using a UV-Vis spectrophotometer at a wavelength of 664 nm to determine the concentration of residual MB in the solution. The pH of MB was controlled in the range of 7-7.8, and the experiment was carried out at a room temperature of 27-30 ℃. This process was done without any replication.

$$\%\ Removal = \left(\frac{C_0 - C_e}{C_0}\right) \times 100$$

where, $C_0$ = initial concentration of MB (mg/L), $C_e$ = equilibrium (final) concentration of MB after adsorption (mg/L).

### 2.4 Adsorption isotherm studies

The adsorption isotherm is the relationship between the distribution of the adsorbent between the adsorbed phase on

the surface and the bulk phase at equilibrium at a certain temperature. The adsorption isotherm is used to obtain information about the type of adsorption and the condition of the adsorbent surface. The adsorption isotherm equations used in this study are the Langmuir adsorption isotherm equation and the Freundlich adsorption isotherm. The type of adsorption can be determined by testing the linear regression equation of the adsorption isotherm, both the Langmuir and the Freundlich models.

The Langmuir isotherm is determined by following the equation:

$$\frac{C_e}{q_e} = \frac{1}{q_m K_L} + \frac{C_e}{q_m} \quad (1)$$

Meanwhile, the Freundlich isotherm is determined by following the equation:

$$Log\ q_e = Log\ K_f + \frac{1}{n} log\ Ce \quad (2)$$

where,

$q_e$ = Amount of substance adsorbed at equilibrium (mg/g)
$C_e$ = Adsorbate concentration at equilibrium (mg/L)
$q_m$ = Maximum adsorption capacity (mg/g)
$K_L$ = Langmuir constant (L/mg)
$K_f$ = Freundlich constant (L/mg)
$n$ = The adsorption intensity constant

## 3. RESULTS AND DISCUSSION

### 3.1 Biochar yield from pyrolyzed *Gnetum gnemon* shell biomass

In this study, biochar was synthesized via the pyrolysis of gnemon shells, a lignocellulosic biomass waste composed primarily of lignin, cellulose, and hemicellulose [20]. The thermal decomposition of these biopolymers during pyrolysis directly influences biochar yield, with temperature variations significantly affecting the final product characteristics.

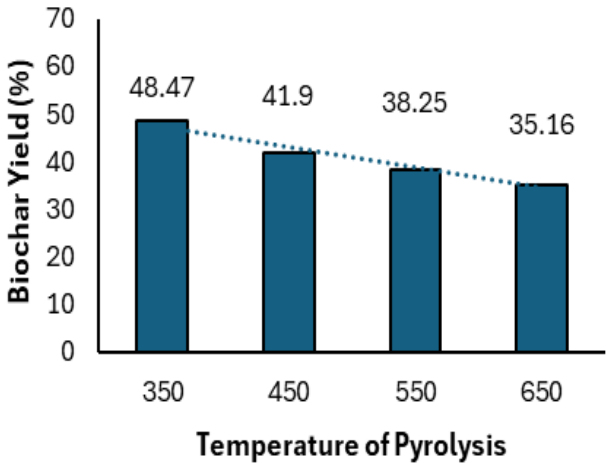


**Figure 1.** Biochar yields from *Gnetum gnemon* shell as a function of pyrolysis temperature

As depicted in Figure 1, biochar yield exhibited a decreasing trend with increasing pyrolysis temperature, attributed to enhanced thermal degradation and volatilization of organic constituents [21]. The most pronounced reduction in yield occurred between 350–450 ℃, decreasing from 48.47% to 41.9% (a decline of 6.57%), whereas at a temperature of 550 ℃, there was a decrease in yield of 3.65% and 3.09% at a temperature of 650 ℃. This substantial loss is primarily associated with the extensive decomposition of cellulose and hemicellulose, as well as the release of bound water molecules [22]. Due to their relatively simple chemical structures and lower thermal stability, cellulose and hemicellulose undergo significant degradation at 250–350 ℃, releasing gaseous byproducts such as carbon monoxide (CO), carbon dioxide ($CO_2$), methane ($CH_4$), and various volatile hydrocarbons [23, 24].

At temperatures exceeding 450 ℃, the decline in biochar yield stabilizes, with Figure 1 showing a smaller yield decline within the same range (3.65% and 3.09% < 6.57%). This indicates that most of the thermal decomposition and volatile release occurred at lower temperatures [25, 26]. In this range (T > 450 ℃), the gradual degradation of lignin contributes to the formation of a thermally stable carbonaceous matrix, thereby mitigating further yield reduction. These findings align with previous studies demonstrating that lignin decomposes over a broader temperature range (200–500 ℃) and plays a crucial role in determining the final carbon content of biochar [27].

### 3.2 Surface morphology

The surface morphology of biochars derived from *gnemon* shells at different pyrolysis temperatures was examined using SEM, as shown in Figure 2. The SEM images reveal a progressive structural transformation with increasing temperature. At 350 ℃ (Figure 2(A)), the biochar largely retains its original biomass characteristics, exhibiting a smooth and compact surface with minimal porosity due to incomplete carbonization and limited tissue devolatilization [28, 29]. As the temperature rises to 450 ℃ (Figure 2(B)), pore formation becomes more evident, with larger, well-defined voids and signs of partial structural collapse. This transition indicates enhanced volatilization of organic components, particularly the thermal degradation of lignin, which typically begins around 400 ℃ [30].

At 550 ℃ (Figure 2(C)), the biochar undergoes a more pronounced transformation, developing an interconnected porous network, which suggests a substantial increase in surface area and pore volume [31, 32]. However, further heating to 650 ℃ (Figure 2(D)) leads to partial pore collapse and fusion, resulting in smaller particle sizes and increased surface roughness due to accelerated carbonization and structural densification [33].

This study demonstrates that pyrolysis temperature plays a crucial role in shaping the morphology and porosity of biochar, which directly influences its adsorption capacity. Since the primary adsorption mechanism of microporous materials relies on the micropore filling effect, the well-developed porous structure and large surface area of gnemon shell biochar may offer abundant adsorption sites for pollutants [27, 34].

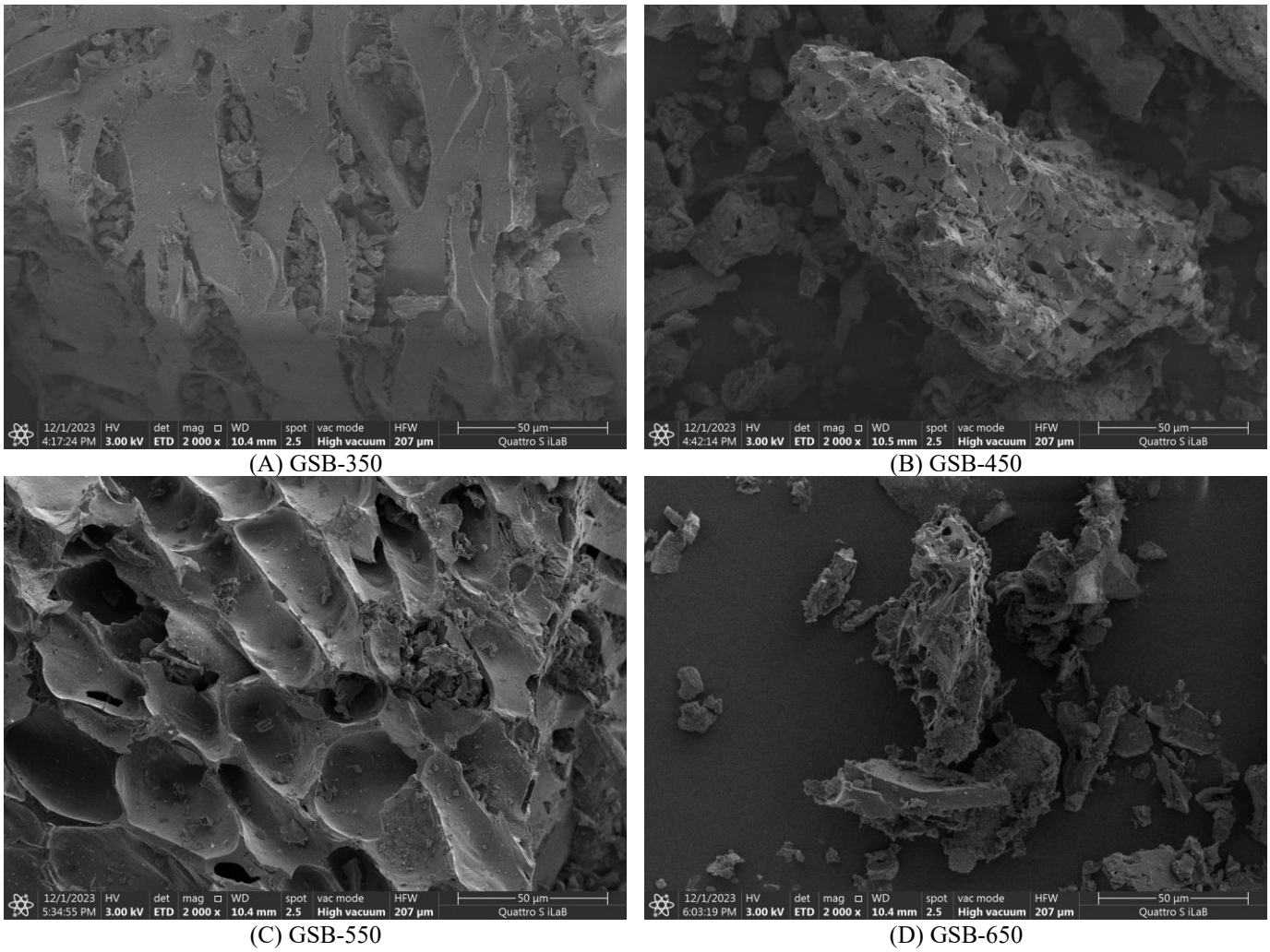


(A) GSB-350 (B) GSB-450

(C) GSB-550 (D) GSB-650

**Figure 2.** Surface morphology of *Gnetum gnemon* shell biochars at different pyrolysis temperatures (A) GSB-350, (B) GSB-450, (C) GSB-550, and (D) GSB-650

### 3.3 Brunauer-Emmett-Teller surface area, pore volume, and average pore radius

The BET surface area, total pore volume, and average pore radius of biochar derived from gnemon shell pyrolysis at various temperatures are presented in Table 1. The data indicate a general trend of increasing BET surface area and total pore volume with rising pyrolysis temperature. At 350 ℃ and 450 ℃, the BET surface area and total pore volume exhibited modest increases from 1.841 $m^2/g$ to 5.640 $m^2/g$ and 0.0302 $cm^3/g$ to 0.0325 $cm^3/g$, respectively. However, at 550 ℃, a more pronounced increase was observed, reaching 23.336 $m^2/g$ for the BET surface area and 0.05 $cm^3/g$ for the total pore volume. A substantial enhancement occurred at 650 ℃, where the BET surface area surged to 137.984 $m^2/g$ (5.9-fold compared with the BET surface area at 550 ℃), and the total pore volume expanded to 0.1197 $cm^3/g$. These results are supported by the SEM analysis shown in Figure 2, which indicates a significant transformation in biochar morphology with increasing pyrolysis temperature.

This finding is in line with walnut shell biochar, where the BET surface area of walnut shell biochar at 500 ℃ is 9 $m^2/g$, increasing to 164 $m^2/g$ (18-fold) at 600 ℃, in addition to beech wood chips biochar at 500 ℃ is 89 $m^2/g$ to 311 (3.5-fold) $m^2/g$ at 600 ℃ [35]. Hickory wood chip biochar at 450 ℃ has a BET surface area of 1.6 $m^2/g$, which increases to 256 $m^2/g$ (160-fold) at a pyrolysis temperature of 600 ℃ [36]. Bamboo biochar at a pyrolysis temperature of 450 ℃ has a BET surface area of 18.2 $m^2/g$ to 470 $m^2/g$ at a pyrolysis temperature of 600 ℃ [37]. Soybean stover biochar at a pyrolysis temperature of 300 ℃ has a BET surface area of 5.61 $m^2/g$ to 420.3 $m^2/g$ at a temperature of 700 ℃, and peanut shell biochar at a pyrolysis temperature of 300 ℃ has a BET surface area of 3.14 $m^2/g$ to 448.2 $m^2/g$ at a temperature of 700 ℃ [38].

**Table 1.** Brunauer-Emmett-Teller (BET) surface area, total pore volume, and average pore radius of *Gnetum gnemon* shell biochar

| Biochar Sample | BET Surface Area ($m^2/g$) | Total Pore Volume ($cm^3/g$) | Average Pore Radius (Å) |
|---|---|---|---|
| GSB-350 | 1.841 | 0.0302 | 329.053 |
| GSB-450 | 5.640 | 0.0325 | 115.209 |
| GSB-550 | 23.336 | 0.0500 | 42.8550 |
| GSB-650 | 137.98 | 0.1197 | 17.3549 |

The dramatic increase in BET surface area at 650 ℃ (Table 1) suggests a potential optimization point for adsorption performance. That while macropores may collapse, micropores and mesopores can still form or become more accessible at higher pyrolysis temperatures, contributing significantly to surface area as measured by nitrogen adsorption. This increase in surface area and porosity is attributed to the degradation of organic constituents, including

cellulose, hemicellulose, and lignin. Additionally, the formation of vascular bundle-like structures during pyrolysis further contributed to biochar porosity [39]. In the 500–600 ℃ range, the rapid decomposition of lignin, accompanied by the release of $H_2$ and $CH_4$, played a pivotal role in the significant enhancement of BET surface area and pore volume [40].

In contrast, increasing the pyrolysis temperature led to a notable reduction in the average pore radius. At 350 ℃, biochar (GSB-350) exhibited an average pore radius of 329.053 Å, indicative of a macroporous structure. However, at 650 ℃, this value drastically declined to 17.3549 Å, signifying the predominance of micropores. Pyrolysis temperatures exceeding 600 ℃ favor micropore development due to extensive lignin decomposition and aromatic condensation reactions, which facilitate volatile release and further pore formation [41]. Furthermore, at elevated temperatures, the thinning of pore walls and the enlargement of internal pore structures promote the formation of additional micropores [42].

These findings underscore the critical role of pyrolysis temperature in modulating biochar porosity. Higher temperatures promote pore formation and surface area expansion through the removal of volatile components, thereby enhancing the suitability of biochar for adsorption applications [43, 44]. The transition from macropores to micropores has a significant impact on adsorption performance. Macropores (> 50 nm) primarily act as transport pathways that facilitate mass transfer, while micropores (< 2 nm) serve as the primary adsorption sites due to their large specific surface area and confinement effect. Therefore, an optimal balance of macropores, mesopores, and micropores is more important than surface area alone for efficient adsorption in practical applications [45, 46].

### 3.4 Functional groups analysis

The FTIR spectra of gnemon shell biochar, presented in Figure 3, illustrate notable transformations in functional groups as pyrolysis temperature increases. At lower temperatures (GSB-350 and GSB-450), the biochar retains a significant presence of oxygen-containing functional groups, particularly the C-O and C-O-C stretching vibrations observed at 1035 $cm^{-1}$ and 991 $cm^{-1}$, which are indicative of residual cellulose and hemicellulose components [47]. These functional groups persist even in higher-temperature biochars (GSB-550 and GSB-650), likely due to their overlap with the silica adsorption region [48]. Notably, the peak at 1035 $cm^{-1}$ sharpens in GSB-650, suggesting increased silica formation at elevated temperatures. This transformation is further corroborated by the emergence of a pronounced Si-O-Si vibration at 435 $cm^{-1}$ in GSB-650, confirming the progressive mineralization of biochar [49].

Additionally, the peak around 1576 $cm^{-1}$, associated with C=C and C=O stretching in aromatic hydrocarbons, diminishes as temperature rises, indicating a shift toward a more condensed aromatic structure with reduced aliphatic content [50]. Furthermore, peaks appearing at approximately 471 $cm^{-1}$ and 539 $cm^{-1}$ may correspond to lattice vibrations of X-M–X and M–X bonds, suggesting the presence of inorganic elements, and M refers to metal such as calcium, magnesium, iron, and manganese within the biochar matrix [51, 52].

In addition to the carbon matrix, the presence of silica and mineral constituents (e.g., Ca, Mg, Fe, Al) plays an important role in modulating the adsorption properties. These inorganic phases are not simply passive fillers; rather, they can act as active sites through mechanisms such as ion exchange, surface complexation, and electrostatic interactions, especially in the adsorption of heavy metals and polar contaminants [53, 54].

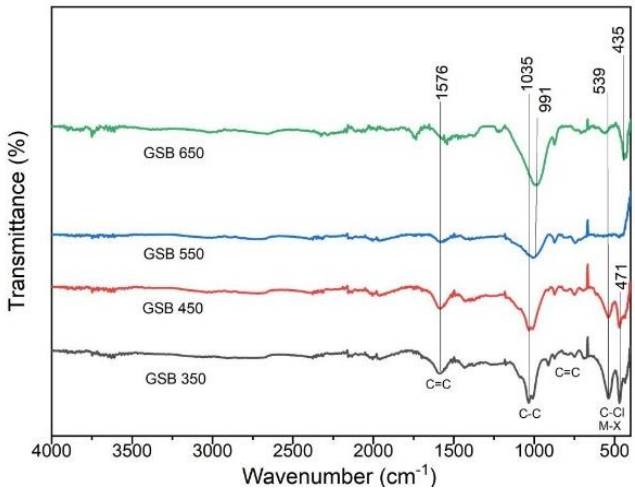


**Figure 3.** Fourier transform infrared (FTIR) spectra of *Gnetum gnemon* shell biochars produced at different pyrolysis temperatures

Overall, these spectral changes highlight the structural evolution of gnemon shell biochar under increasing pyrolysis temperatures. The data suggest a transition from an organic, oxygen-rich composition at lower temperatures to a thermally stabilized, mineral-rich material with a highly carbonized framework at higher temperatures.

### 3.5 X-ray diffraction analysis

The structural evolution of gnemon shell biochar at different pyrolysis temperatures was analyzed using XRD, with the resulting patterns shown in Figure 4.

The diffraction profiles exhibit a broad peak around $2\theta = 22°$, indicating the low crystallinity and amorphous nature of carbon [55]. As the pyrolysis temperature increases, this peak narrows and becomes more pronounced, suggesting the progressive ordering of carbon structures [56]. This transformation is attributed to the formation and evolution of turbostratic crystallites, where graphene-like layers remain misaligned but become more organized [57]. The increased structural ordering enhances the material's surface characteristics, potentially improving adsorption performance by increasing accessible surface area, creating more defined pore structures, and facilitating π–π interactions with adsorbates [58].

Additionally, distinct peaks emerge at $2\theta = 26.6°$ and 29.5°, corresponding to $SiO_2$ and $CaCO_3$, respectively [59]. These peaks intensify at higher pyrolysis temperatures, particularly in GSB-550 and GSB-650, indicating enhanced particle growth and increased crystallization of mineral components within the biochar matrix [60, 61]. This structural evolution suggests that higher pyrolysis temperatures promote both carbon ordering and inorganic crystallization, influencing the biochar's physicochemical properties.

The formation of $SiO_2$ and $CaCO_3$ crystals during pyrolysis can affect surface functionality, both positively and negatively. $SiO_2$ can increase surface hydrophilicity and stability, providing additional sites for interaction with polar molecules [62]. Similarly, $CaCO_3$ can increase surface basicity, which

favors the adsorption of acidic species [63]. On the other hand, excessive crystallization of these minerals can clog pores, reduce surface area, or mask more reactive carbon sites, thus limiting adsorption efficiency [64].

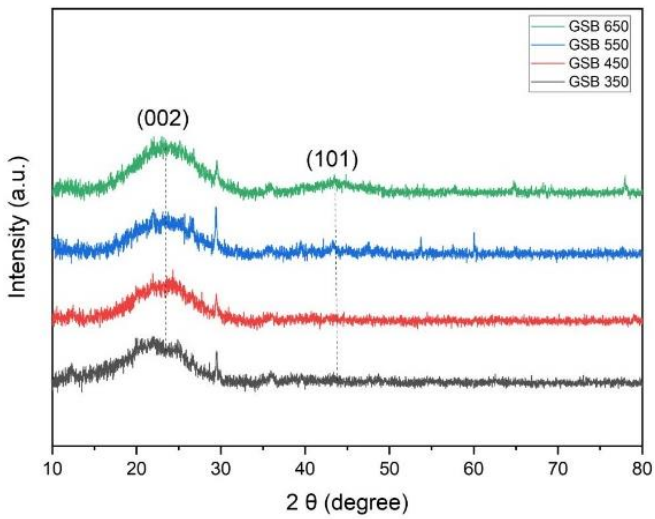


**Figure 4.** X-ray diffraction (XRD) patterns of *Gnetum gnemon* shell biochar produced at different pyrolysis temperatures

### 3.6 Thermal decomposition and stability of *Gnetum gnemon* shell-derived biochar

The thermal stability of gnemon shell-derived biochar was analyzed using thermogravimetric analysis (TGA), as shown in Figure 5. Differences in weight loss at various pyrolysis temperatures indicate distinct levels of carbonization and structural transformation. An initial weight reduction of 2–5% occurred between 0–150 ℃, primarily due to the evaporation of residual moisture and physically adsorbed water [65, 66]. Beyond this, biochars produced at 350°C (GSB-350) and 450 ℃ (GSB-450) experienced additional mass loss of ~3–5% in the 150–400 ℃ range, likely caused by the decomposition of hemicellulose and volatile organic compounds [67].

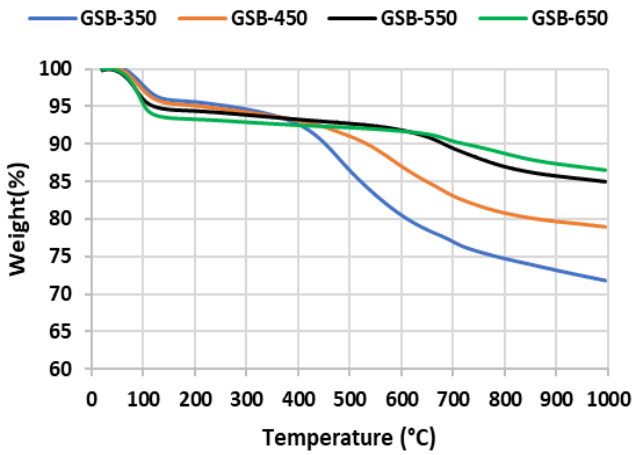


**Figure 5.** Thermogravimetric Analysis (TGA) curve of *Gnetum gnemon* shell biochar at different pyrolysis temperatures

A more substantial weight loss was observed between 400 and 1000°C, with GSB-350 and GSB-450 losing 21% and 14% of their mass, respectively. This continued degradation is attributed to the decomposition of lignin, which remains in biochar produced at lower pyrolysis temperatures. Lignin is known for its higher thermal stability compared to cellulose and hemicellulose, leading to its gradual breakdown at elevated temperatures [24, 61].

In contrast, GSB-550 and GSB-650 followed a two-stage degradation pattern, with a steady weight reduction from 150 to 650 ℃, followed by a more gradual decline beyond 650 ℃. This trend suggests that higher pyrolysis temperatures promote a more complete transformation, resulting in a stable carbon structure with enhanced thermal resistance [62].

Overall, the results confirm that increasing pyrolysis temperature improves biochar stability by enhancing carbonization and reducing the proportion of volatile compounds. Biochars produced at 550 ℃ and 650 ℃ demonstrated superior thermal resistance, making them more suitable for applications requiring high-temperature durability. Furthermore, this enhanced thermal stability also significantly contributes to the functional durability of biochar in adsorption and reuse scenarios. High-temperature biochar with a more ordered carbon structure and low volatile content tends to withstand harsh regeneration conditions, including high-temperature treatment, oxidative environments, or repeated adsorption–desorption cycles. This allows the material to maintain its structural integrity and adsorption capacity over multiple cycles, making it a more reliable candidate for long-term and industrial-scale applications [68].

### 3.7 Proximate and ultimate analysis of biochar

The proximate and ultimate compositions of biochar derived from *gnemon* shell at different pyrolysis temperatures are summarized in Tables 2 and 3. As shown in Table 2, the proximate analysis reveals significant compositional changes with increasing temperature. While these trends are generally observed in biochar production, the magnitude of these changes can be influenced by the characteristics of the feedstock, in this case, gnemon shell. Volatile matter content decreases from 34.65% at 350 ℃ to 7.13% at 650 ℃, consistent with the decomposition of cellulose and hemicellulose at higher temperatures, leading to a more carbon-rich material [69]. Conversely, fixed carbon content increases, reaching a maximum of 69.86% at 650 ℃, indicating advanced carbonization and enhanced structural integrity [53, 70]. These findings align with previous studies showing that as pyrolysis temperature increases, volatile matter content declines while fixed carbon content rises [71-73]. The increased structural ordering enhances the material's surface characteristics, potentially improving adsorption performance by increasing accessible surface area, creating more defined pore structures, and facilitating π–π interactions with adsorbates [58].

On the other hand, ash and moisture contents exhibit non-linear trends. Ash content increases with pyrolysis temperature, peaking at 21.06% at 550 ℃. This trend can be attributed to the progressive concentration of inorganic constituents and the accumulation of combustion residues from organic matter degradation [74, 75]. However, at 650 ℃, the ash content decreases to 16.49%, likely due to the volatilization of certain mineral components at elevated temperatures, particularly alkali metals in the form of chlorides or oxides [76].

**Table 2.** Moisture content, ash content, volatile matter, and fixed carbon values of *Gnetum gnemon* shell biochar

| Sample | Moisture Content | Ash Content | Volatile Matter | Fixed Carbon |
|---|---|---|---|---|
| | (%) | | | |
| GSB-350 | 5.19 | 12.50 | 34.65 | 47.66 |
| GSB-450 | 4.76 | 13.59 | 17.67 | 63.98 |
| GSB-550 | 4.12 | 21.06 | 10.94 | 63.88 |
| GSB-650 | 6.52 | 16.49 | 7.13 | 69.86 |

Interestingly, moisture content follows a different pattern, decreasing from 5.19% at 350 ℃ to 4.12% at 550 ℃. This reduction is driven by higher thermal energy at elevated temperatures, which accelerates water evaporation, breaks hydroxyl bonds that release bound water, and induces structural modifications that render the biochar more hydrophobic, reducing its ability to retain moisture [77]. However, at 650 ℃, the moisture content unexpectedly rises to 6.52%. This increase may be attributed to the development of a more extensive network of micropores in the biochar structure at higher temperatures, as confirmed by BET analysis, which enhances its capacity to adsorb moisture from the surrounding environment through capillary condensation [78].

**Table 3.** Elemental composition of *Gnetum gnemon* shell biochar from ultimate analysis

| Sample | Carbon (C) | Hydrogen (H) | Nitrogen (N) | Sulfur (S) | Oxygen (O) |
|---|---|---|---|---|---|
| | | | % wt | | |
| GSB-350 | 67.84 | 3.80 | 0.94 | 0.21 | 14.03 |
| GSB-450 | 72.34 | 3.06 | 0.66 | 0.18 | 9.49 |
| GSB-550 | 69.03 | 2.24 | 0.74 | 0.17 | 5.86 |
| GSB-650 | 74.36 | 1.43 | 0.51 | 0.12 | 5.93 |

The ultimate analysis (Table 3) reveals the elemental composition (C, H, N, S, O) of the biochar, providing insights into its chemical transformation at increasing pyrolysis temperatures. Carbon content progressively increases from 67.84% at 350 ℃ to 74.36% at 650 ℃, while the proportions of hydrogen, oxygen, nitrogen, and sulfur decrease.

The carbon content generally increases with increasing pyrolysis temperature, which is attributed to the progressive removal of volatile compounds and the enrichment of fixed carbon. However, a slight decrease was observed at 550 ℃. This behavior may be associated with structural reorganization at intermediate pyrolysis temperatures, the release of residual volatile carbon compounds, and the relative increase in ash content. Where GSB-550 has an ash content 21.06%, the highest compared to other biochars. At higher temperatures (650 ℃), the carbon content increases again due to enhanced carbonization and aromatization, resulting in a more stable carbon structure. This result is in line with several studies where carbon content increases, then decreases slightly, then increases again, this occurs in walnut shell biochar [35], wheat straw biochar [79], Miscatanthus and swichgrass biochar [40] and chicken manure [80], where Carbon content increases with increasing pyrolysis temperature, but at a certain temperature there is a slight decrease then increases again.

The nitrogen content declines due to the volatilization of $NH_4$-N and $NO_3$-N species at moderate temperatures (~200 ℃), while some nitrogen is retained in more stable pyridine and pyrrole configurations at elevated temperatures [81, 82]. Sulfur content follows a similar decreasing trend as sulfur-containing volatiles are released, particularly around 350 ℃ [61, 83].

Moreover, the H and O contents declined from 3.80% at 350 ℃ to 1.43% at 650 ℃ and from 14.03% at 350 ℃ to 5.93% at 650 ℃, respectively. This suggests that the degree of carbonization increases significantly at higher pyrolysis temperatures, accompanied by dehydration, deoxidation reactions, and the breakdown of weak oxygenated bonds within the biochar structure [29, 84].

Based on ultimate analysis, key atomic ratios such as (O+N)/C, H/C, and O/C were calculated as shown in Table 4, as they serve as indicators of biochar polarity, hydrophilicity, and aromaticity, respectively. A higher (O+N)/C and O/C ratios suggest greater polarity and hydrophilicity, while a lower H/C ratio is indicative of increased aromaticity [85]. In this study, these ratios decreased progressively with rising pyrolysis temperatures, indicating that biochar becomes more aromatic, carbon-rich, and hydrophobic, while its polarity diminishes [86].

**Table 4.** Atomic ratios of *Gnetum gnemon* shell biochar from ultimate analysis

| Sample | H/C | O/C | (O+N)/C |
|---|---|---|---|
| | | % wt | |
| GSB-350 | 0.056 | 0.206 | 0.220 |
| GSB-450 | 0.042 | 0.131 | 0.140 |
| GSB-550 | 0.032 | 0.085 | 0.096 |
| GSB-650 | 0.003 | 0.080 | 0.087 |

The unexpected increase in water content observed at 650 °C deserves more critical discussion. Typically, higher pyrolysis temperatures reduce hydrophilic functional groups (e.g., –OH, –COOH), leading to a lower affinity for water [87]. However, this anomaly may reflect not only intrinsic surface chemistry but also external factors such as environmental humidity during storage and handling. Highly porous biochars, especially those with well-developed micropores and mesopores, can act as sponges, passively absorbing atmospheric moisture upon cooling and exposure to air [88, 89]. Furthermore, although high-temperature pyrolysis decreases specific surface functionalities, it can leave behind an open pore network that enhances water vapor physisorption [90]. Thus, the water absorption observed at 650 ℃ is most likely due to the combined effects of texture evolution and environmental exposure rather than a direct contradiction to the expected hydrophobicity trend.

### 3.8 Methylene blue adsorption performance

The effect of initial MB concentration on removal capacity is shown in Figure 6, where biochar with different pyrolysis temperatures exhibits different responses. Based on Figure 6, the removal capacity decreases with increasing initial MB concentration across 4 types of biochar. Furthermore, the higher the pyrolysis temperature, the higher the removal capacity, with GSB-650 providing the highest at each initial

MB concentration, while GSB-350 provides the lowest. The removal capacity of GSB-650 is 1.2-2.4 times greater than that of GSB-350.

The adsorption capacity at various initial MB concentrations is displayed in Figure 7. The adsorption capacity increases with the pyrolysis temperature. GSB-650 biochar has the highest adsorption capability across all concentrations, while GSB-350 has the lowest. According to the calculation results, all biochars' adsorption capacities ($q_e$) increased with increasing initial MB concentration from 20 to 60 mg/L, then decreased at 80 mg/L.

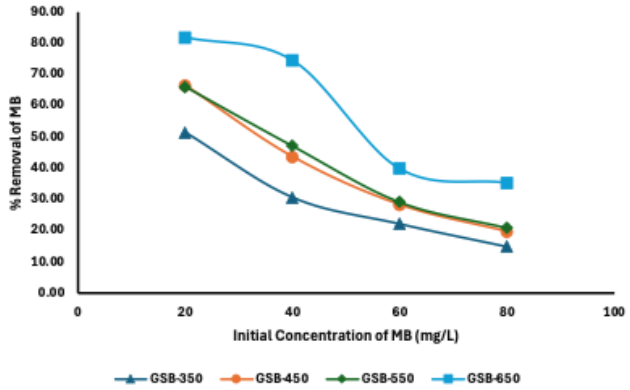


**Figure 6.** Effect of initial methylene blue (MB) concentration on the removal capacities of the four biochars

Higher removal capacity of GSB-650 was revealed because this biochar has a much higher specific surface area, 137.98 $m^{2}/g$ (compared with other biochars). BET results show the surface area of GSB-650 is 74.9 times larger than GSB-350, 24times larger than GSB-450, and 5.9 times larger than GSB-550. The larger surface area contains more available adsorption sites, so that MB molecules can exhibit better interaction with the biochar matrix. The specific surface area and pore structure are generalized characteristics of biochar that have a direct dependency on the number of available adsorption sites [91, 92].

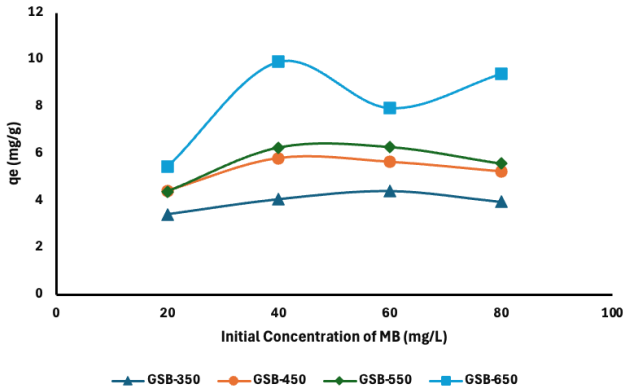


**Figure 7.** Adsorption capacities of the four biochar types

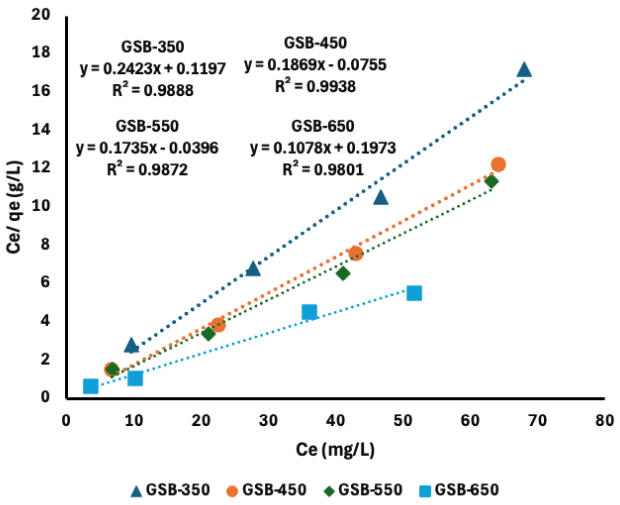


**Figure 8.** Langmuir isotherm graph

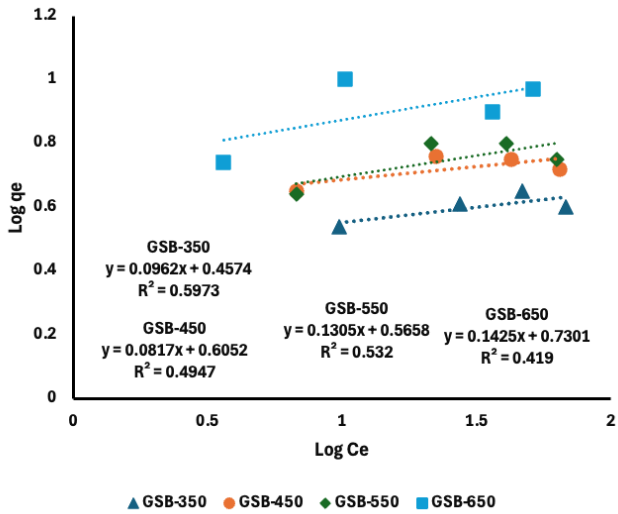


**Figure 9.** Freundlich isotherm graph

Lower FTIR bands for the MB adsorption process were presented in biochar obtained at higher pyrolysis temperatures (650 °C), because they had surface functional groups providing more support to this process. The peak at 1734 $cm^{-1}$, which corresponds to carbonyl groups (C=O), and the peak at 970 $cm^{-1}$, which belongs to the C–O group. It also showed the appearance of a more developed aromatic structure peak at 872 $cm^{-1}$. The presence of these functional groups enhances the interaction between adsorbate and adsorbent, mainly by means of π-π interactions between the aromatic structure of biochar and aromatic ring in MB molecule [93, 94], as well as formed by electrostatic interactions and hydrogen bonds with oxygenic groups [38, 95].

Therefore, the high MB adsorption capacity on 650 °C biochar is assisted by not only its higher surface area (BET results), but also a more developed aromatic structure and organic functional groups, which are favorable for various adsorption mechanisms [93, 95]. On the contrary, the adsorption capacity of biochar produced at lower temperatures is relatively low owing to its less developed carbon structure and the non-optimal distribution of functional groups [38, 94].

Data from XRD indicated that $SiO_2$ and $CaCO_3$ peaks began to appear, with an increasing intensity at $2\theta = 26.6°$ and 29.5°, when the burning temperature was raised, especially in GSB-550 and GSB-650. It showed that higher pyrolysis temperatures favored the inorganic minerals to crystallize in the biochar matrix. Even if a high density of crystallized $SiO_2$ and $CaCO_3$ could possibly over-bulk pores, decrease the available surface or cover reactive carbon sites, the adsorption results in this study indicate that these negative effects are not prevalent. The Langmuir maximum adsorption capacity even progressed from a value of 4.13 mg/g (GSB-350) to 9.28 mg/g (GSB-650), which illustrates how the increase in temperature favored MB adsorption rather than hindering it by the

structural evolution process.

The rise in $q_e$ values at higher initial concentrations refers to the fact that the absorption capacity is directly proportional to the amount of adsorbate in a solution. At 20 mg/L, the number of MB molecules is very low and therefore, the interfacial interaction between adsorbate and sorbent still remains limited. This gives rise to a comparatively small $q_e$ value. Since the initial concentrations are increased to 40 and 60 mg/L MB molecules in the environment, which means that there are more opportunities for these molecules to interact with the biochar surface. This condition enhances the driving force or energy of adsorption, which finally results in an improvement in adsorption capacity. It is confirmed by adhesivity theory that, as the initial concentration increases, the mass transfer between the solution and the adsorbent surface will be more rapid due to a higher degree of concentration gradient [96-98].

For $q_e$, it was found that at 80 mg/L, the values for most of the adsorbents performed a downward trend, which showed that the adsorption system began to deviate from ideal conditions. Some reasons responsible for this reduction may be the saturation of active sites on the adsorbent surface, competition between MB molecules for limited sites, and inhibition of diffusion in biochar pores. Adsorption capacity may also be reduced at high concentrations due to the possibility. This phenomenon suggests that, at higher concentrations, adsorption mechanisms are altered, and the traditional assumptions of classical isotherm theory can no longer be applied [93]. This will also be in line with the isotherm model.

Figures 8 and 9 show the fitting curves of the MB adsorption capacity of GSB-350, GSB-450, GSB-550, and GSB-650 with the Langmuir and the Freundlich isotherm models. The $R^2$ values for both the Freundlich and Langmuir models were fairly good but better for MB adsorption (around 0.9) when fitted using the Langmuir isotherm and not the Freunidch model (at least with an output that displayed a good fit). This follows our previous assumption that the Langmuir model describes monolayer adsorption onto a surface with a finite number of identical sites, which is common for this type of data [99]. The Freundlich isotherm is an empirical model that describes adsorption on heterogeneous surfaces with a non-uniform distribution of adsorption energy and is applicable to multilayer adsorption processes [93, 94].

**Table 5.** Langmuir adsorption isotherm constants for methylene blue (MB) adsorption using the *Gnetum gnemon* shell biochar

| Biochar Types | Langmuir Model | | |
|---|---|---|---|
| | $q_m$ (mg/g) | $K_L$ (L/mg) | $R^2$ |
| GSB-350 | 4.13 | 2.02 (valid) | 0.9888 |
| GSB-450 | 5.35 | −2.48 (no valid) | 0.9938 |
| GSB-550 | 5.76 | −4.38 (no valid) | 0.9872 |
| GSB-650 | 9.28 | 0.55 (valid) | 0.9801 |

Nevertheless, from Table 5 and Figures 8 and 9, we can see that the Langmuir model showed better values as compared to the Freundlich model, but it is more accurate from a physical point of view since negative values were found for GSB-450 and GSB-550. This suggests that the basic assumptions of the Langmuir model are not completely fulfilled in this research. On the other hand, the Freundlich model also gave a lower value, showing a bad fit to experimental data. This result suggests that the adsorption system is complicated and cannot be sufficiently explained by the classical isotherm model [94].

## 4. CONCLUSIONS

This study highlights the important role of pyrolysis temperature in adjusting the physicochemical properties and adsorption capacity of *gnemon* shell biochar. The biochar yield decreased from 48.47% (350 °C) to 35.16% (650 °C), while the surface area and pore volume increased sharply (1.84 to 137.98 $m^2/g$ (74.9-fold); 0.0302 to 0.1197 $cm^3/g$ (3.9-fold). FTIR and XRD confirmed progressive aromatization, loss of oxygenated groups, and mineral crystallization, which were supported by TGA, proximate, and ultimate analyses. The increase in carbon content (74.36%), decrease in H/C ratio (0.003) and O/C ratio (0.080), and increase in fixed carbon (69.86%) indicated improved stability and hydrophobicity. Adsorption tests showed a maximum MB removal (9.28 mg/g) at GSB-650, Isothermal matching with Langmuir-type monolayer chemisorption. Overall, Gnemon shell biochar is a promising low-cost adsorbent for dye removal. Due to its low efficiency, activation or functionalization is required to improve performance and expand its applications in environmental remediation.

## REFERENCES


[1] Tavassoli, S., Carbonara, N. (2014). The role of knowledge variety and intensity for regional innovation. Small Business Economics, 43(2): 493-509. https://doi.org/10.1007/s11187-014-9547-7

[2] Miao, Z., Baležentis, T., Tian, Z., Shao, S., Geng, Y., Wu, R. (2019). Environmental performance and regulation effect of China's atmospheric pollutant emissions: Evidence from "Three Regions and Ten Urban Agglomerations". Environmental and Resource Economics, 74(1): 211-242. https://doi.org/10.1007/s10640-018-00315-6

[3] Dutta, S., Adhikary, S., Bhattacharya, S., Roy, D., Chatterjee, S., Chakraborty, A., Banerjee, D., Ganguly, A., Nanda, S., Rajak, P. (2024). Contamination of textile dyes in aquatic environment: Adverse impacts on aquatic ecosystem and human health, and its management using bioremediation. Journal of Environmental Management, 353: 120103. https://doi.org/10.1016/j.jenvman.2024.120103

[4] Miranda, E.C., Prado, P.G., Leon-Velarde, C. (2024). A systematic review of polluting processes produced by the textile industry and proposals for abatement methods. Textile & Leather Review, 7: 88-103. https://doi.org/10.31881/tlr.2023.165

[5] Alisha, Kumar, S. (2024). Textile dyeing effluents: Challenges, characterization, and sustainable treatment. In Advances in Renewable Natural Materials for Textile Sustainability, pp. 263-273.

[6] Oladoye, P.O., Ajiboye, T.O., Omotola, E.O., Oyewola, O.J. (2022). Methylene blue dye: Toxicity and potential elimination technology from wastewater. Results in Engineering, 16: 100678. https://doi.org/10.1016/j.rineng.2022.100678

[7] Tkaczyk, A., Mitrowska, K., Posyniak, A. (2020). Synthetic organic dyes as contaminants of the aquatic environment and their implications for ecosystems: A review. Science of The Total Environment, 717: 137222.

https://doi.org/10.1016/j.scitotenv.2020.137222
[8] Khan, S., Malik, A. (2017). Toxicity evaluation of textile effluents and role of native soil bacterium in biodegradation of a textile dye. Environmental Science and Pollution Research, 25(5): 4446-4458. https://doi.org/10.1007/s11356-017-0783-7
[9] Teixeira, Y.N., Filho, F.J.d.P., Bacurau, V.P., Menezes, J.M.C., Fan, A.Z., Melo, R.P.F. (2022). Removal of Methylene Blue from a synthetic effluent by ionic flocculation. Heliyon, 8(10): e10868. https://doi.org/10.1016/j.heliyon.2022.e10868
[10] Kalaycıoğlu, Z., Uysal, B.Ö., Pekcan, Ö., Erim, F.B. (2023). Efficient photocatalytic degradation of methylene blue dye from aqueous solution with cerium oxide nanoparticles and graphene oxide-doped polyacrylamide. ACS Omega, 8(14): 13004-13015. https://doi.org/10.1021/acsomega.3c00198
[11] Liu, Y., Ke, Y., Shang, Q., Yang, X., Wang, D., Liao, G. (2022). Fabrication of multifunctional biomass-based aerogel with 3D hierarchical porous structure from waste reed for the synergetic adsorption of dyes and heavy metal ions. Chemical Engineering Journal, 451: 138934. https://doi.org/10.1016/j.cej.2022.138934
[12] Pan, X., Gu, Z., Chen, W., Li, Q. (2021). Preparation of biochar and biochar composites and their application in a Fenton-like process for wastewater decontamination: A review. Science of The Total Environment, 754: 142104. https://doi.org/10.1016/j.scitotenv.2020.142104
[13] Bui, T.K., Nguyen, L.T., Cao, T.M., Van Pham, V. (2024). Surface modification of biochar for removal of dye from industrial effluent: A green approach to mitigate environmental pollutants. Catalytic Applications of Biochar for Environmental Remediation: A Green Approach Towards Environment Restoration, 1478: 1-21. https://doi.org/10.1021/bk-2024-1478.ch001
[14] Zhou, R., Zhang, M., Shao, S. (2022). Optimization of target biochar for the adsorption of target heavy metal ion. Scientific Reports, 12(1): 1-17. https://doi.org/10.1038/s41598-022-17901-w
[15] Prahasti, G., Edikresnha, D., Rezeki, Y.A., Munir, M.M., Khairurrijal, K. (2019). The synthesis and characterization of composite Electrospun fibers of polyvinylpyrrolidone and shell extract of Melinjo (Gnetum gnemon L.). Materials Today: Proceedings, 13: 187-192. https://doi.org/10.1016/j.matpr.2019.03.212
[16] Slamet, Yuliusman, Dwijayanti, A., Kartika, S. (2020). Characteristics of activated carbon from Melinjo shells composed of TiO2 nanoparticles. Journal of Physics: Conference Series, 1477(5): 052012. https://doi.org/10.1088/1742-6596/1477/5/052012
[17] Raj, A., Yadav, A., Arya, S., Sirohi, R., Kumar, S., Rawat, A.P., Thakur, R.S., Patel, D.K., Bahadur, L., Pandey, A. (2021). Preparation, characterization and agri applications of biochar produced by pyrolysis of sewage sludge at different temperatures. Science of The Total Environment, 795: 148722. https://doi.org/10.1016/j.scitotenv.2021.148722
[18] Zhang, P., Li, Y., Cao, Y., Han, L. (2019). Characteristics of tetracycline adsorption by cow manure biochar prepared at different pyrolysis temperatures. Bioresource Technology, 285: 121348. https://doi.org/10.1016/j.biortech.2019.121348
[19] Zhang, G., Zhang, Q., Sun, K., Liu, X., Zheng, W., Zhao, Y. (2011). Sorption of simazine to corn straw biochars prepared at different pyrolytic temperatures. Environmental Pollution, 159(10): 2594-2601. https://doi.org/10.1016/j.envpol.2011.06.012
[20] Dwijayanti, A., Kartika, S., Yuliusman. (2019). The effect of carbonization temperature and activator to the characteristics of melinjo shell (Gnetum genom) activated carbon. AIP Conference Proceedings, 2175(1): 020057. https://doi.org/10.1063/1.5134621
[21] Khater, E., Bahnasawy, A., Hamouda, R., Sabahy, A., Abbas, W., Morsy, O.M. (2024). Biochar production under different pyrolysis temperatures with different types of agricultural wastes. Scientific Reports, 14(1): 1-8. https://doi.org/10.1038/s41598-024-52336-5
[22] He, X., Liu, Z., Niu, W., Yang, L., Zhou, T., Qin, D., Niu, Z., Yuan, Q. (2018). Effects of pyrolysis temperature on the physicochemical properties of gas and biochar obtained from pyrolysis of crop residues. Energy, 143: 746-756. https://doi.org/10.1016/j.energy.2017.11.062
[23] Hu, M., Chen, Z., Wang, S., Guo, D., Ma, C., Zhou, Y., Chen, J., Laghari, M., Fazal, S., Xiao, B., Zhang, B., Ma, S. (2016). Thermogravimetric kinetics of lignocellulosic biomass slow pyrolysis using distributed activation energy model, Fraser-Suzuki deconvolution, and iso-conversional method. Energy Conversion and Management, 118: 1-11. https://doi.org/10.1016/j.enconman.2016.03.058
[24] Yang, H., Yan, R., Chen, H., Lee, D. H., Zheng, C. (2007). Characteristics of hemicellulose, cellulose and lignin pyrolysis. Fuel, 86(12-13): 1781-1788. https://doi.org/10.1016/j.fuel.2006.12.013
[25] Shen, Z., Hou, D., Jin, F., Shi, J., Fan, X., Tsang, D.C., Alessi, D.S. (2019). Effect of production temperature on lead removal mechanisms by rice straw biochars. Science of The Total Environment, 655: 751-758. https://doi.org/10.1016/j.scitotenv.2018.11.282
[26] Suliman, W., Harsh, J.B., Abu-Lail, N.I., Fortuna, A., Dallmeyer, I., Garcia-Perez, M. (2016). Influence of feedstock source and pyrolysis temperature on biochar bulk and surface properties. Biomass and Bioenergy, 84: 37-48. https://doi.org/10.1016/j.biombioe.2015.11.010
[27] Zhang, X., Zhang, P., Yuan, X., Li, Y., Han, L. (2020). Effect of pyrolysis temperature and correlation analysis on the yield and physicochemical properties of crop residue biochar. Bioresource Technology, 296: 122318. https://doi.org/10.1016/j.biortech.2019.122318
[28] Claoston, N., Samsuri, A., Husni, M.A., Amran, M. (2014). Effects of pyrolysis temperature on the physicochemical properties of empty fruit bunch and rice husk biochars. Waste Management & Research: The Journal for a Sustainable Circular Economy, 32(4): 331-339. https://doi.org/10.1177/0734242x14525822
[29] Luo, Q., Deng, Y., Li, Y., He, Q., Wu, H., Fang, X. (2024). Effects of pyrolysis temperatures on the structural properties of straw biochar and its adsorption of tris-(1-chloro-2-propyl) phosphate. Scientific Reports, 14(1): 1-14. https://doi.org/10.1038/s41598-024-77299-5
[30] Gaur, L., Poonia, P. (2024). Optimization, characterisation and evaluation of biochar obtained from biomass of invasive weed *Crotalaria burhia*. Nature Environment and Pollution Technology, 23(4): 1995-2008. https://doi.org/10.46488/nept.2024.v23i04.008
[31] Guo, J., Lua, A.C. (1998). Characterization of chars pyrolyzed from oil palm stones for the preparation of

activated carbons. Journal of Analytical and Applied Pyrolysis, 46(2): 113-125. https://doi.org/10.1016/s0165-2370(98)00074-6
[32] Leng, L., Xiong, Q., Yang, L., Li, H., Zhou, Y., Zhang, W., Jiang, S., Li, H., Huang, H. (2021). An overview on engineering the surface area and porosity of biochar. Science of The Total Environment, 763: 144204. https://doi.org/10.1016/j.scitotenv.2020.144204
[33] Elnour, A.Y., Alghyamah, A.A., Shaikh, H.M., Poulose, A.M., Al-Zahrani, S.M., Anis, A., Al-Wabel, M.I. (2019). Effect of pyrolysis temperature on biochar microstructural evolution, physicochemical characteristics, and its influence on biochar/polypropylene composites. Applied Sciences, 9(6): 1149. https://doi.org/10.3390/app9061149
[34] Sun, J., Zhang, Z., Ji, J., Dou, M., Wang, F. (2017). Removal of Cr6+ from wastewater via adsorption with high-specific-surface-area nitrogen-doped hierarchical porous carbon derived from silkworm cocoon. Applied Surface Science, 405: 372-379. https://doi.org/10.1016/j.apsusc.2017.02.044
[35] Wystalska, K., Kwarciak-Kozłowska, A. (2021). The effect of biodegradable waste pyrolysis temperatures on selected biochar properties. Materials, 14(7): 1644. https://doi.org/10.3390/ma14071644
[36] Ding, Z., Wan, Y., Hu, X., Wang, S., Zimmerman, A.R., Gao, B. (2016). Sorption of lead and methylene blue onto hickory biochars from different pyrolysis temperatures: Importance of physicochemical properties. Journal of Industrial and Engineering Chemistry, 37: 261-267. https://doi.org/10.1016/j.jiec.2016.03.035
[37] Yao, Y., Gao, B., Zhang, M., Inyang, M., Zimmerman, A.R. (2012). Effect of biochar amendment on sorption and leaching of nitrate, ammonium, and phosphate in a sandy soil. Chemosphere, 89(11): 1467-1471. https://doi.org/10.1016/j.chemosphere.2012.06.002
[38] Ahmad, M., Lee, S.S., Dou, X., Mohan, D., Sung, J., E Yang, J., Ok, Y.S. (2012). Effects of pyrolysis temperature on soybean stover- and peanut shell-derived biochar properties and TCE adsorption in water. Bioresource Technology, 118: 536-544. https://doi.org/10.1016/j.biortech.2012.05.042
[39] Li, M., Liu, Q., Guo, L., Zhang, Y., Lou, Z., Wang, Y., Qian, G. (2013). Cu(II) removal from aqueous solution by Spartina alterniflora derived biochar. Bioresource Technology, 141: 83-88. https://doi.org/10.1016/j.biortech.2012.12.096
[40] Chatterjee, R., Sajjadi, B., Chen, W., Mattern, D.L., Hammer, N., Raman, V., Dorris, A. (2020). Effect of pyrolysis temperature on physicochemical properties and acoustic-based amination of biochar for efficient $CO_2$ adsorption. Frontiers in Energy Research, 8: 85. https://doi.org/10.3389/fenrg.2020.00085
[41] Chen, Y., Yang, H., Wang, X., Zhang, S., Chen, H. (2012). Biomass-based pyrolytic polygeneration system on cotton stalk pyrolysis: Influence of temperature. Bioresource Technology, 107: 411-418. https://doi.org/10.1016/j.biortech.2011.10.074
[42] Li, X., Liu, H., Liu, N., Sun, Z., Fu, S., Zhan, X., Yang, J., Zhou, R., Zhang, H., Zhang, J., Han, X. (2023). Pyrolysis temperature had effects on the physicochemical properties of biochar. Plant, Soil and Environment, 69(8): 363-373. https://doi.org/10.17221/444/2022-pse
[43] Zhang, L., Ren, Y., Xue, Y., Cui, Z., Wei, Q., Han, C., He, J. (2020). Preparation of biochar by mango peel and its adsorption characteristics of Cd(ii) in solution. RSC Advances, 10(59): 35878-35888. https://doi.org/10.1039/d0ra06586b
[44] Wang, H., Yang, Y., Wang, M., Yuan, R., Song, W., Wang, L., Liang, N., Shi, J., Li, J. (2024). Insights into the roles of surface functional groups and micropores in the sorption of ofloxacin on banana pseudo-stem biochars. Sustainability, 16(7): 2629. https://doi.org/10.3390/su16072629
[45] Wu, L., Li, Y., Fu, Z., Su, B. (2020). Hierarchically structured porous materials: Synthesis strategies and applications in energy storage. National Science Review, 7(11): 1667-1701. https://doi.org/10.1093/nsr/nwaa183
[46] Sayed, M.S., Aman, D., Fayed, M.G., Omran, M.M., Zaki, T., Mohamed, S.G. (2024). Unravelling the role of pore structure of biomass-derived porous carbon in charge storage mechanisms for supercapacitors. RSC Advances, 14(34): 24631-24642. https://doi.org/10.1039/d4ra04681a
[47] Xiao, X., Chen, B., Zhu, L. (2014). Transformation, morphology, and dissolution of silicon and carbon in rice straw-derived biochars under different pyrolytic temperatures. Environmental Science & Technology, 48(6): 3411-3419. https://doi.org/10.1021/es405676h
[48] Magdziarz, A., Wilk, M., Gajek, M., Nowak-Woźny, D., Kopia, A., Kalemba-Rec, I., Koziński, J.A. (2016). Properties of ash generated during sewage sludge combustion: A multifaceted analysis. Energy, 113: 85-94. https://doi.org/10.1016/j.energy.2016.07.029
[49] Gbouri, I., Yu, F., Wang, X., Wang, J., Cui, X., Hu, Y., Yan, B., Chen, G. (2022). Co-pyrolysis of sewage sludge and wetland biomass waste for biochar production: Behaviors of phosphorus and heavy metals. International Journal of Environmental Research and Public Health, 19(5): 2818. https://doi.org/10.3390/ijerph19052818
[50] Jin, J., Li, Y., Zhang, J., Wu, S., Cao, Y., Liang, P., Zhang, J., Wong, M.H., Wang, M., Shan, S., Christie, P. (2016). Influence of pyrolysis temperature on properties and environmental safety of heavy metals in biochars derived from municipal sewage sludge. Journal of Hazardous Materials, 320: 417-426. https://doi.org/10.1016/j.jhazmat.2016.08.050
[51] Prakongkep, N., Gilkes, R.J., Wiriyakitnateekul, W. (2015). Forms and solubility of plant nutrient elements in tropical plant waste biochars. Journal of Plant Nutrition and Soil Science, 178(5): 732-740. https://doi.org/10.1002/jpln.201500001
[52] Zhang, M., Gao, B., Yao, Y., Inyang, M. (2013). Phosphate removal ability of biochar/MgAl-LDH ultra-fine composites prepared by liquid-phase deposition. Chemosphere, 92(8): 1042-1047. https://doi.org/10.1016/j.chemosphere.2013.02.050
[53] Inyang, M., Gao, B., Yao, Y., Xue, Y., Zimmerman, A. R., Pullammanappallil, P., Cao, X. (2012). Removal of heavy metals from aqueous solution by biochars derived from anaerobically digested biomass. Bioresource Technology, 110: 50-56. https://doi.org/10.1016/j.biortech.2012.01.072
[54] Park, J., Ok, Y.S., Kim, S., Cho, J., Heo, J., Delaune, R.D., Seo, D. (2016). Competitive adsorption of heavy metals onto sesame straw biochar in aqueous solutions. Chemosphere, 142: 77-83.

https://doi.org/10.1016/j.chemosphere.2015.05.093
[55] Gurav, R., Bhatia, S.K., Choi, T., Choi, Y., Kim, H.J., Song, H., Lee, S.M., Park, S.L., Lee, H.S., Koh, J., Jeon, J., Yoon, J., Yang, Y. (2021). Application of macroalgal biomass derived biochar and bioelectrochemical system with Shewanella for the adsorptive removal and biodegradation of toxic azo dye. Chemosphere, 264: 128539. https://doi.org/10.1016/j.chemosphere.2020.128539
[56] Setiawan, H., Sakamoto, M., Fujisaki, T., Lyth, S.M., Shiratori, Y. (2022). Development of a sustainable nitrogen-doped biochar desulfurizer for solid oxide fuel cell systems. Biomass and Bioenergy, 167: 106631. https://doi.org/10.1016/j.biombioe.2022.106631
[57] Keiluweit, M., Nico, P.S., Johnson, M.G., Kleber, M. (2010). Dynamic molecular structure of plant biomass-derived black carbon (biochar). Environmental Science & Technology, 44(4): 1247-1253. https://doi.org/10.1021/es9031419
[58] Cheng, Y., Wang, B., Shen, J., Yan, P., Kang, J., Wang, W., Bi, L., Zhu, X., Li, Y., Wang, S., Shen, L., Chen, Z. (2022). Preparation of novel N-doped biochar and its high adsorption capacity for atrazine based on π-π electron donor-acceptor interaction. Journal of Hazardous Materials, 432: 128757. https://doi.org/10.1016/j.jhazmat.2022.128757
[59] Tan, L., Ma, Z., Yang, K., Cui, Q., Wang, K., Wang, T., Wu, G., Zheng, J. (2020). Effect of three artificial aging techniques on physicochemical properties and Pb adsorption capacities of different biochars. Science of The Total Environment, 699: 134223. https://doi.org/10.1016/j.scitotenv.2019.134223
[60] Shaaban, A., Se, S., Dimin, M., Juoi, J.M., Husin, M.H.M., Mitan, N.M.M. (2014). Influence of heating temperature and holding time on biochars derived from rubber wood sawdust via slow pyrolysis. Journal of Analytical and Applied Pyrolysis, 107: 31-39. https://doi.org/10.1016/j.jaap.2014.01.021
[61] Cantrell, K.B., Hunt, P.G., Uchimiya, M., Novak, J.M., Ro, K.S. (2012). Impact of pyrolysis temperature and manure source on physicochemical characteristics of biochar. Bioresource Technology, 107: 419-428. https://doi.org/10.1016/j.biortech.2011.11.084
[62] Gomes, O.P., Rheinheimer, J.P.C., Dias, L.F.G., Batagin-Neto, A., Lisboa-Filho, P.N. (2022). Revisiting the hydroxylation phenomenon of SiO2: A study through "hard-hard" and "soft-soft" interactions. Journal of Molecular Modeling, 28(5): 1-10. https://doi.org/10.1007/s00894-022-05107-w
[63] Manyatshe, A., Sibali, L.L. (2025). A review on egg waste-based adsorbents for the removal of organic and inorganic contaminants from aqueous solution. Heliyon, 11(3): e42278. https://doi.org/10.1016/j.heliyon.2025.e42278
[64] Speranza, G. (2019). The role of functionalization in the applications of carbon materials: An overview. C-Journal of Carbon Research, 5(4): 84. https://doi.org/10.3390/c5040084
[65] Santos, L.B., Striebeck, M.V., Crespi, M.S., Ribeiro, C.A., De Julio, M. (2015). Characterization of biochar of pine pellet. Journal of Thermal Analysis and Calorimetry, 122(1): 21-32. https://doi.org/10.1007/s10973-015-4740-8
[66] Om Prakash, M., Raghavendra, G., Panchal, M., Ojha, S. (2020). Thermogravimetric analysis of biochar from Arhar fiber powder prepared at different pyrolysis temperatures. In Innovative Product Design and Intelligent Manufacturing Systems: Select Proceedings of ICIPDIMS 2019, pp. 429-437. https://doi.org/10.1007/978-981-15-2696-1_42
[67] Sun, Y., Gao, B., Yao, Y., Fang, J., Zhang, M., Zhou, Y., Chen, H., Yang, L. (2014). Effects of feedstock type, production method, and pyrolysis temperature on biochar and hydrochar properties. Chemical Engineering Journal, 240: 574-578. https://doi.org/10.1016/j.cej.2013.10.081
[68] Kan, X., Suo, Y., Shi, B., Zheng, Y., Liu, Z., Ma, W., Li, X., Zhang, J. (2025). Synergistic enhancement of rhodamine B adsorption by coffee shell biochar through high-temperature pyrolysis and water washing. Molecules, 30(13): 2769. https://doi.org/10.3390/molecules30132769
[69] Kim, W., Shim, T., Kim, Y., Hyun, S., Ryu, C., Park, Y., Jung, J. (2013). Characterization of cadmium removal from aqueous solution by biochar produced from a giant Miscanthus at different pyrolytic temperatures. Bioresource Technology, 138: 266-270. https://doi.org/10.1016/j.biortech.2013.03.186
[70] Setyawan, H.Y., Sunyoto, N.M.S., Sugiarto, Y., Dewanti, B.S.S.D., et al. (2024). Characterisation of biochar from various carbon sources. BIO Web of Conferences, 90: 06003. https://doi.org/10.1051/bioconf/20249006003
[71] Intani, K., Latif, S., Cao, Z., Müller, J. (2018). Characterisation of biochar from maize residues produced in a self-purging pyrolysis reactor. Bioresource Technology, 265: 224-235. https://doi.org/10.1016/j.biortech.2018.05.103
[72] Alghamdi, A.G., Aljohani, B.H., Aly, A.A. (2021). Impacts of olive waste-derived biochar on hydro-physical properties of sandy soil. Sustainability, 13(10): 5493. https://doi.org/10.3390/su13105493
[73] Albalasmeh, A.A., Quzaih, M.Z., Gharaibeh, M.A., Rusan, M., Mohawesh, O.E., Rababah, S.R., Alqudah, A., Alghamdi, A.G., Naserin, A. (2024). Significance of pyrolytic temperature, application rate and incubation period of biochar in improving hydro-physical properties of calcareous sandy loam soil. Scientific Reports, 14(1): 1-13. https://doi.org/10.1038/s41598-024-57755-y
[74] Cao, X., Harris, W. (2010). Properties of dairy-manure-derived biochar pertinent to its potential use in remediation. Bioresource Technology, 101(14): 5222-5228. https://doi.org/10.1016/j.biortech.2010.02.052
[75] Chen, T., Zhang, Y., Wang, H., Lu, W., Zhou, Z., Zhang, Y., Ren, L. (2014). Influence of pyrolysis temperature on characteristics and heavy metal adsorptive performance of biochar derived from municipal sewage sludge. Bioresource Technology, 164: 47-54. https://doi.org/10.1016/j.biortech.2014.04.048
[76] Zhao, S., Ta, N., Wang, X. (2017). Effect of temperature on the structural and physicochemical properties of biochar with apple tree branches as feedstock material. Energies, 10(9): 1293. https://doi.org/10.3390/en10091293
[77] Setyawan, H.Y., Safira, L., Mulyarto, A.R., Wijana, S., Pranowo, D. (2023). The effect of pyrolysis temperature and ball-milling duration on characteristics of micro bio-char derived from oil palm empty fruit bunches. Sustainable Environment, 9(1): 2173041. https://doi.org/10.1080/27658511.2023.2173041

[78] Mclennon, E., Solomon, J.K., Neupane, D., Davison, J. (2020). Biochar and nitrogen application rates effect on phosphorus removal from a mixed grass sward irrigated with reclaimed wastewater. Science of The Total Environment, 715: 137012. https://doi.org/10.1016/j.scitotenv.2020.137012

[79] Zhang, X., Yang, X., Yuan, X., Tian, S., Wang, X., Zhang, H., Han, L. (2022). Effect of pyrolysis temperature on composition, carbon fraction and abiotic stability of straw biochars: Correlation and quantitative analysis. Carbon Research, 1(1): 1-14. https://doi.org/10.1007/s44246-022-00017-1

[80] Domingues, R.R., Trugilho, P.F., A Silva, C., A De Melo, I.C.N., A Melo, L.C., Magriotis, Z.M., A Sánchez-Monedero, M. (2017). Properties of biochar derived from wood and high-nutrient biomasses with the aim of agronomic and environmental benefits. PLOS ONE, 12(5): e0176884. https://doi.org/10.1371/journal.pone.0176884

[81] Bagreev, A., Bandosz, T.J., Locke, D.C. (2001). Pore structure and surface chemistry of adsorbents obtained by pyrolysis of sewage sludge-derived fertilizer. Carbon, 39(13): 1971-1979. https://doi.org/10.1016/s0008-6223(01)00026-4

[82] Enders, A., Hanley, K., Whitman, T., Joseph, S., Lehmann, J. (2012). Characterization of biochars to evaluate recalcitrance and agronomic performance. Bioresource Technology, 114: 644-653. https://doi.org/10.1016/j.biortech.2012.03.022

[83] Al-Wabel, M.I., Al-Omran, A., El-Naggar, A.H., Nadeem, M., Usman, A.R. (2013). Pyrolysis temperature induced changes in characteristics and chemical composition of biochar produced from conocarpus wastes. Bioresource Technology, 131: 374-379. https://doi.org/10.1016/j.biortech.2012.12.165

[84] Demirbas, A. (2004). Effects of temperature and particle size on bio-char yield from pyrolysis of agricultural residues. Journal of Analytical and Applied Pyrolysis, 72(2): 243-248. https://doi.org/10.1016/j.jaap.2004.07.003

[85] Chen, B., Zhou, D., Zhu, L. (2008). Transitional adsorption and partition of nonpolar and polar aromatic contaminants by biochars of pine needles with different pyrolytic temperatures. Environmental Science & Technology, 42(14): 5137-5143. https://doi.org/10.1021/es8002684

[86] Fu, P., Yi, W., Bai, X., Li, Z., Hu, S., Xiang, J. (2011). Effect of temperature on gas composition and char structural features of pyrolyzed agricultural residues. Bioresource Technology, 102(17): 8211-8219. https://doi.org/10.1016/j.biortech.2011.05.083

[87] Roshan, A., Ghosh, D., Maiti, S.K. (2023). How temperature affects biochar properties for application in coal mine spoils? A meta-analysis. Carbon Research, 2(1): 1-17. https://doi.org/10.1007/s44246-022-00033-1

[88] Zhao, S., Ta, N., Wang, X. (2020). Absorption of Cu(II) and Zn(II) from aqueous solutions onto biochars derived from apple tree branches. Energies, 13(13): 3498. https://doi.org/10.3390/en13133498

[89] Mukherjee, A., Zimmerman, A., Harris, W. (2011). Surface chemistry variations among a series of laboratory-produced biochars. Geoderma, 163(3-4): 247-255. https://doi.org/10.1016/j.geoderma.2011.04.021

[90] Ju, J., You, K., Liu, S., She, Y., Zou, C. (2022). Effect of water vapor on pore structure, surface functional groups, and combustion performance of pyrolytic semicoke. ACS Omega, 7(28): 24587-24595. https://doi.org/10.1021/acsomega.2c02396

[91] Al-Asadi, S.T., Mussa, Z.H., Al-Qaim, F.F., Kamyab, H., Al-Saedi, H.F.S., Deyab, I.F., Kadhim, N.J. (2025). A comprehensive review of methylene blue dye adsorption on activated carbon from edible fruit seeds: A case study on kinetics and adsorption models. Carbon Trends, 20: 100507. https://doi.org/10.1016/j.cartre.2025.100507

[92] Wang, J., Tan, Y., Yang, H., Zhan, L., Sun, G., Luo, L. (2023). On the adsorption characteristics and mechanism of methylene blue by ball mill modified biochar. Scientific Reports, 13(1): 1-12. https://doi.org/10.1038/s41598-023-48373-1

[93] Tan, X., Liu, Y., Zeng, G., Wang, X., Hu, X., Gu, Y., Yang, Z. (2015). Application of biochar for the removal of pollutants from aqueous solutions. Chemosphere, 125: 70-85. https://doi.org/10.1016/j.chemosphere.2014.12.058

[94] Wang, J., Wang, S. (2019). Preparation, modification and environmental application of biochar: A review. Journal of Cleaner Production, 227: 1002-1022. https://doi.org/10.1016/j.jclepro.2019.04.282

[95] Li, H., Dong, X., da Silva, E.B., de Oliveira, L.M., Chen, Y., Ma, L.Q. (2017). Mechanisms of metal sorption by biochars: Biochar characteristics and modifications. Chemosphere, 178: 466-478. https://doi.org/10.1016/j.chemosphere.2017.03.072

[96] Ho, Y., McKay, G. (1999). Pseudo-second order model for sorption processes. Process Biochemistry, 34(5): 451-465. https://doi.org/10.1016/s0032-9592(98)00112-5

[97] Yetgin, S., Amlani, M. (2024). Agricultural low-cost waste adsorption of methylene blue and modelling linear isotherm method versus nonlinear prediction. Clean Technologies and Environmental Policy, 27(3): 1205-1225. https://doi.org/10.1007/s10098-024-02928-6

[98] Bu, Z., Fang, Y., Chen, H., Zhang, M., Wang, F. (2025). Study on the adsorption properties of organically modified diatomite for methylene blue. Scientific Reports, 15(1): 27561. https://doi.org/10.1038/s41598-025-13768-9

[99] Ayawei, N., Ebelegi, A.N., Wankasi, D. (2017). Modelling and interpretation of adsorption isotherms. Journal of Chemistry, 2017: 1-11. https://doi.org/10.1155/2017/3039817